RESEARCH ARTICLE

Adsorption of magnetic manganese ferrites to simulated monomeric mercury in flue gases

Lei Sun[1‡], **Xiajun Zhang**[2‡], **Zhou Wang**[3*], **Min Liu**[2*]

1 Danyang Maternal and Child Health Hospital, Zhenjiang, P.R. China, **2** The People's Hospital of Danyang, Affiliated Danyang Hospital of Nantong University, Zhenjiang, P.R. China, **3** Vanadium and Titanium Resource Comprehensive Utilization Key Laboratory of Sichuan Province, School of Vanadium and Titanium, Panzhihua University, Panzhihua, P.R. China

‡ LS and XZ are contributed equally to this work as share first authorship.
* dyliumin@126.com (ML); pzhwangzhou@163.com (ZW)

Abstract

Magnetic $MnFe_2O_4$ nanoparticles were successfully prepared by the rapid combustion method at 500 ˚C for 2 h with 30 mL absolute ethanol, and were characterized by SEM, TEM, XRD, VSM, and XPS techniques, their average particle size and the saturation magnetization were about 25.3 nm and 79.53 $A{\cdot}m^2/kg$, respectively. The magnetic $MnFe_2O_4$ nanoparticles were employed in a fixed bed experimental system to investigate the adsorption capacity of Hg^0 from air. The $MnFe_2O_4$ nanoparticles exhibited the large adsorption performance on Hg^0 with the adsorption capacity of 16.27 μg/g at the adsorption temperature of 50 ˚C with the space velocity of 4.8×10^4 h^{-1}. The VSM and EDS results illustrated that the prepared $MnFe_2O_4$ nanoparticles were stable before and after adsorption and successfully adsorbed Hg^0. The TG curves demonstrated that the mercury compound formed after adsorption was HgO, and both physical and chemical adsorption processes were observed. Magnetic $MnFe_2O_4$ nanoparticles revealed excellent adsorbance of Hg^0 in air, which suggested that $MnFe_2O_4$ nanoparticles be promising for the removal of Hg^0.

Citation: Sun L, Zhang X, Wang Z, Liu M (2024) Adsorption of magnetic manganese ferrites to simulated monomeric mercury in flue gases. PLoS ONE 19(6): e0304333. https://doi.org/10.1371/journal.pone.0304333

Editor: Abbas Farmany, Hamadan University of Medical Sciences, ISLAMIC REPUBLIC OF IRAN

Received: February 2, 2024

Accepted: May 10, 2024

Published: June 14, 2024

Data Availability Statement: All relevant data are within the manuscript and its Supporting information files.

Funding: Vanadium and Titanium Resource Comprehensive Utilization Key Laboratory of Sichuan Province (Grant No. 2020FTSZ14).

Competing interests: The authors have declared that no competing interests exist.

1. Introduction

Mercury is harmful to ecosystems because of its long-range transport, persistence, and bioaccumulation [1–3]. Mercury can undergo various stages of transformation to produce methylmercury (MeHg), a highly toxic form of mercury, the ingestion of which can have adverse effects on human health [4]. The increasing concentration of mercury in the environment has attracted the attention of governments and environmental organizations, and has become a worldwide environmental problem. The Minamata Convention on mercury, which entered into force in 2017, emphasizes cost-effective abatement and efficient decontamination of mercury pollution, as well as the sound management and utilization of mercury-rich waste [5]. Coal-fired power plants are reported to be the most significant source of mercury emissions, so in response to this problem, the Emission Standards for Air Pollutants from Power Plants (GB 132232011), published in July 2011, for the first-time limit mercury emission concentrations to no more than 0.03 mg/m^3 of mercury and mercury compounds from coal-fired power plants [6].

Mercury in coal combustion flue gas exists in three main forms: elemental mercury (Hg^0), oxidized mercury (Hg^{2+}), and particulate bound mercury (Hg^P) [7–9]. Hg^{2+} is water soluble and volatile, can be readily adsorbed and removed via a wet scrubber process. Hg^P is susceptible to adsorption and charging, it has a short residence time in the atmosphere, and it is easily removed by electric precipitators. Since Hg^0 is highly volatile and almost insoluble in water, where it remains in the atmosphere for 0.5–2 years. More importantly, Hg^0 is one of the most difficult form to control, and it is challenging to remove mercury from coal-fired flue gases [10].

Catalysis and adsorption methods are the main methods for the removal of elemental mercury [11–14]. In recent years, various catalysts and adsorbents have been reported for mercury removal, such as activated carbon, precious metals, and metal oxides [8, 15, 16]. Among them, magnetic ferrite nanomaterials are a new type of material that offers the advantages of easy separation, recyclability, and environmental friendliness, so they have been widely applied in organic and biological separations. Especially, they are excellent adsorbents due to their large specific surface area, abundant active sites, and interfacial effect [17–19]. Simultaneously, manganese oxides can impact the mercury cycle by adsorbing it, influencing the ambient redox potential and regulating microorganism activity. Therefore, $MnFe_2O_4$ is recognized as an excellent adsorbent for removing singlet Hg from coal-fired flue gases. To enhance the removal performance of $MnFe_2O_4$ nanoparticles, researchers have proposed several constructive ideas, such as applying organic or inorganic layers to coat the surface of nanomaterials [20–22], modifying the structural composition and morphology parameters [23], and doping transition metals [24].

Various approaches are available for the preparation of magnetic nanomaterials, such as co-precipitation [25], hydrothermal methods [26], rapid combustion methods [27], and so on. The birdnesting and the nonuniformity of composition are the largest problem owing to the accession of precipitant. While, magnetic nanoparticles prepared by hydrothermal method have long cycle time and small yield. The rapid combustion method has a short preparation cycle, low cost, safe, reliable, and environmentally friendly process, it is easy to produce industrially, and it can achieve the purpose of controlling the sizes and properties of magnetic nanoparticles by changing the amount of solvent and calcination temperature [28–30]. And the application of adsorbents prepared by this method for the removal of elemental mercury from coal combustion flue gas has not been reported.

In this paper, magnetic $MnFe_2O_4$ nanomaterials were prepared from metal nitrates by a rapid combustion method based on the ability of manganese compounds to oxidize mercury, and the factors (volume of anhydrous ethanol and calcination temperature) affecting their adsorption properties were optimized. The mercury removal performance of the magnetic $MnFe_2O_4$ nanomaterials was evaluated in a fixed bed system. Combined with vibrating sample magnetometry (VSM), energy dispersive spectroscopy (EDS) mapping, and thermogravimetric (TG) curves, the mercury removal process was analyzed.

2. Experiment details

2.1 Preparation and characterization of magnetic $MnFe_2O_4$ nanoparticles

Magnetic $MnFe_2O_4$ nanoparticles were prepared via the rapid combustion process, typically, $Fe(NO_3)_3 \cdot 9H_2O$ and $Mn(NO_3)_2 \cdot 6H_2O$ were dissolved into 30 mL absolute ethanol according to 1:2 molar ratio of them to form a homogeneous solution, ignited and burned until extinguished, and calcinated at 400–800 ˚C for 2 h with the heating rate of 3 ˚C/min to obtain magnetic $MnFe_2O_4$ nanoparticles. In the rapid combustion process, anhydrous ethanol acted as both a dispersant and a fuel, effectively dispersing the solute while serving as a catalyst for combustion. The product obtained at the end of the combustion of the solution incompletely formed $MnFe_2O_4$ crystals in a sol state. Subsequently, the semi-finished product was transferred to the temperature-controlled furnace programmed for high-temperature calcination. The purpose of this process was to provide sufficient heat for inducing the formation of $MnFe_2O_4$ nanoparticles and removed impurities such as activated carbon and nitrate.

The microscopic morphology and elemental distribution of $MnFe_2O_4$ nanomaterials were characterized by scanning electron microscopy (SEM), transmission electron microscopy (TEM), and energy dispersive spectroscopy (EDS). The physical phase and crystallinity were analyzed through X-ray diffractometer (XRD). Vibrating sample magnetometer (VSM) was employed to measure the hysteresis loops of $MnFe_2O_4$ nanoparticles before and after adsorption. The formation of the products in the adsorption process was determined by a thermogravimetric curve (TG).

2.2 Elemental mercury adsorption experiments

The actual coal combustion flue gas contains a variety of gases such as N_2, CO_2, O_2, and SO_2. The influence of the various gases on the removal of mercury was complex, and considering that most of the flue gas was N_2, only N_2 was chosen for the experiments (Fig 1). The gas flow rate was controlled by a rotameter and adjusted according to the experimental requirements. Various concentrations of mercury vapors were produced by means of a heated mercury permeation tube. The adsorbent was packed in a U-shaped tube with an inner diameter of 5 mm. To prevent the adsorbent from falling or being blown up by the gas, cotton was inserted at both ends for support and fixation. All experimental piping and connections were made of poly tetra fluoroethylene (PTFE). The tail gas after the reaction is purified with 10% H_2SO_4-4% $KMnO_4$ absorption solution and discharged. Once adsorbed, the solid nanoparticles were

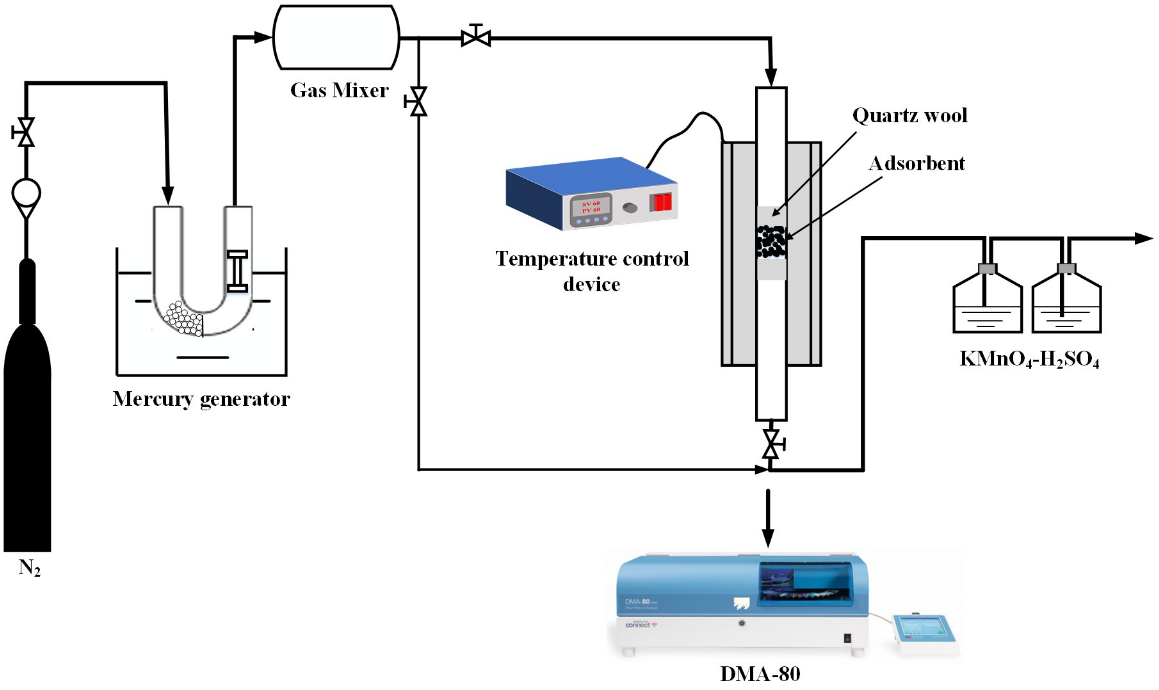

Fig 1. Simple diagram of a fixed bed experimental setup.

https://doi.org/10.1371/journal.pone.0304333.g001

detected by means of DMA-80 mercury analyzer. The experimental data were obtained after three experiments.

3. Results and discussion

3.1 Characterization of magnetic $MnFe_2O_4$ nanoparticles

Fig 2 showed the SEM morphology, TEM image, XRD pattern, and XPS spectra of the $MnFe_2O_4$ nanomaterials calcinated at 500 ˚C for 2 h with 30 mL absolute ethanol. As shown in Fig 2A (S1 Fig), the morphology of the prepared $MnFe_2O_4$ nanomaterials exhibited a granular shape with an average particle size of about 25.3 nm. The TEM image was shown in Fig 2B (S2 Fig), the measured morphology was granular and the average particle size was also around 25.3 nm, which was in general agreement with the observation from SEM morphology. The excellent nano-size made the adsorption capacity extraordinarily large, making it an excellent choice for absorbing Hg^0. XRD pattern of $MnFe_2O_4$ nanoparticles was shown in Fig 2C (S3

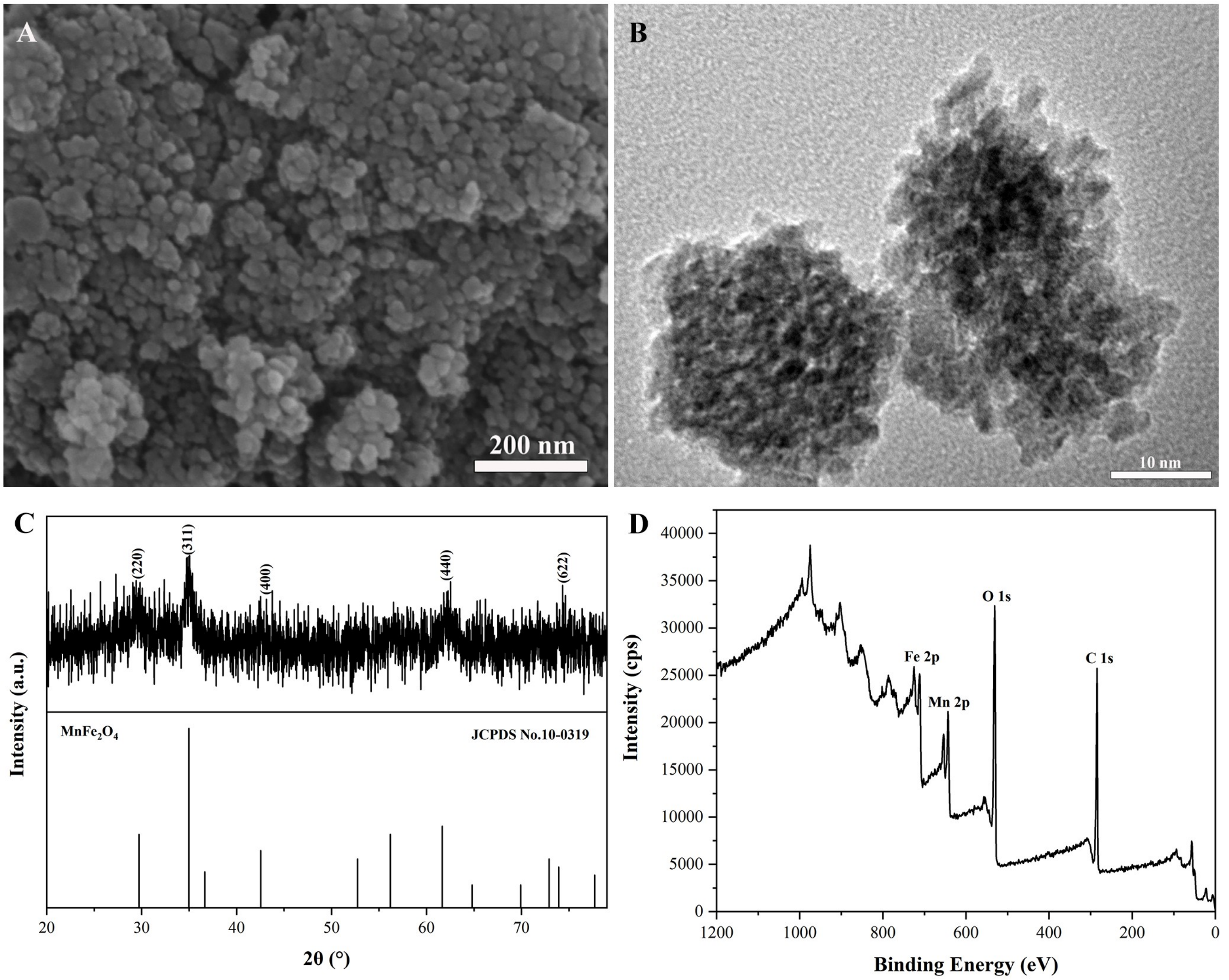

Fig 2. (A) SEM morphology, (B) TEM image, (C) XRD pattern, and (D) XPS spectra of magnetic $MnFe_2O_4$ nanoparticles obtained by calcination at 500 ˚C for 30 mL of absolute ethanol for 2 h.

https://doi.org/10.1371/journal.pone.0304333.g002

Fig), the characteristic peaks were 29.62˚, 34.82˚, 43.13˚, 62.29˚, and 74.34˚, corresponding to the (220), (311), (400), (440), and (622) crystalline planes of the $MnFe_2O_4$ standard card (JCPDS No. 10–0319), which proved that the $MnFe_2O_4$ nanoparticles were prepared successfully [31]. The prepared nanomaterials possessed four components, Mn, Fe, O, and C, as could be seen from the XPS maps (Fig 2D, S4 Fig), which again demonstrated the successful preparation of $MnFe_2O_4$ nanoparticles.

3.2 Effects of preparation factors for $MnFe_2O_4$ nanoparticles on Hg^0 adsorption

To understand the effect of $MnFe_2O_4$ nanoparticles prepared with different alcohol volumes and calcination temperatures on the performance of the mercury removal, it was investigated by a fixed bed experimental system [32].

Anhydrous ethanol was essential in the rapid combustion process, which not only played a role in distributing to the solute and ignition, but also effectively controlled the duration of combustion. As could be seen from Fig 3A (S1 Table), when experimental conditions were controlled at permeation temperature of 40 ˚C, space velocity of 4.8×10^4 h^{-1}, and adsorption temperature of 30 ˚C, the adsorption capacity of Hg^0 increased slowly with the volume of alcohol for the preparation of $MnFe_2O_4$ nanoparticles increasing of from 15 mL to 25 mL, and when the absolute alcohol volume rose to 30 mL, a significant increase of the adsorption capacity could be seen. The reason for this phenomenon might be that the large volume of anhydrous ethanol caused the solute to be dispersed excessively in the solvent, resulting in the formation of smaller grain sizes. However, as the volume of anhydrous ethanol increased further, the adsorption capacity tended to decrease. This might be attributed that the large amount of anhydrous ethanol dispersed the solute, while also prolonging the combustion time. As a result, there was a greater degree of sintering, leading to larger grain size and decreases in specific surface area and adsorption capacity [33]. Therefore, 30 mL was chosen as the optimum volume of absolute alcohol.

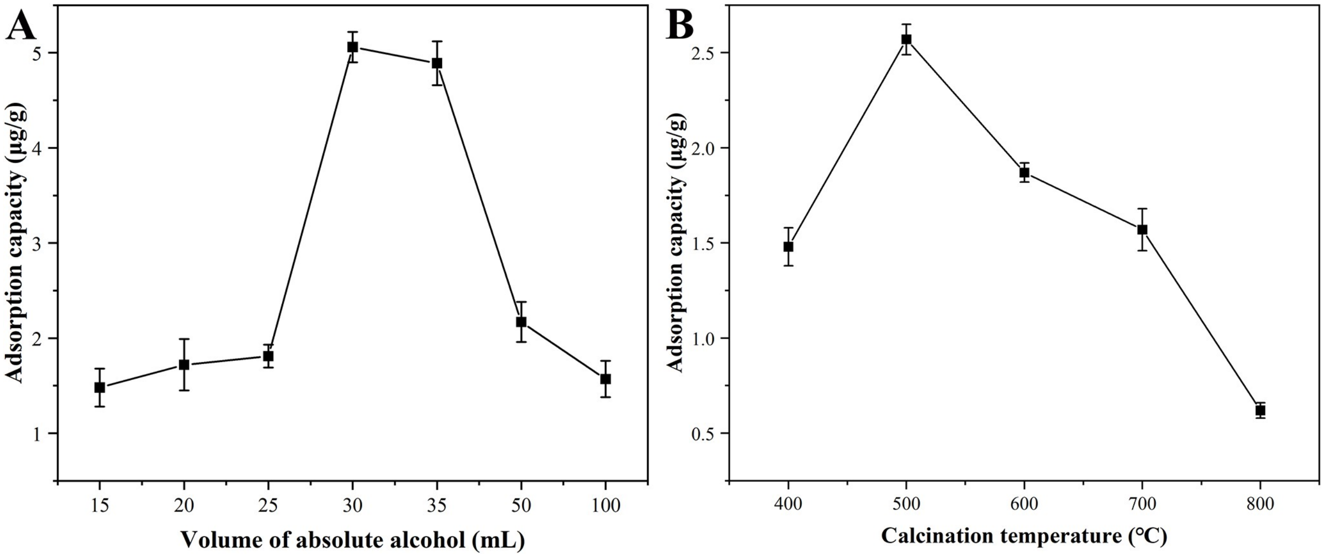

Fig 3. Adsorption curves of Hg^0 by $MnFe_2O_4$ nanoparticles prepared at different calcination temperatures (B) with various alcohol volumes (A) under permeation temperature of 40 ˚C, space velocity of 4.8×10^4 h^{-1}, and adsorption temperature of 30 ˚C.

https://doi.org/10.1371/journal.pone.0304333.g003

Fig 3B (S2 Table) showed the adsorption capacities of $MnFe_2O_4$ nanoparticles prepared at different calcination temperatures for Hg^0 under permeation temperature of 40 ˚C, space velocity of 4.8×10^4 h^{-1}, and adsorption temperature of 30 ˚C. As could be seen from the figures, the adsorption capacity increased with the increase of calcination temperature, reached the maximum adsorption capacity of 2.57 μg/g for $MnFe_2O_4$ nanoparticles calcinated at 500 ˚C, and then reduces. From previous experience, it could be seen that the crystallinity of the produced nanoparticle was poor at 400 ˚C of calcination temperature. And when the calcination temperature was increased to 500 ˚C, the crystallinity improved greatly and the grain size was relatively small. The growth rate of the grains increased with the increase of the calcination temperature, and the crystallinity and grain size also increased, which in turn led to a decrease of specific surface area and a reduction of adsorption capacity [30]. Therefore, 500 ˚C was chosen as the optimum calcination temperature. In summary, the $MnFe_2O_4$ nanoparticles were prepared with alcohol volume of 30 mL and a calcination temperature of 500 ˚C for subsequent adsorption experiments.

3.3 Influence of adsorption temperature on the performance of Hg^0 removal

As could be seen from Fig 4 (S3 Table), when the permeation temperature and space velocity were controlled at 40 ˚C and 4.8×10^4 h^{-1}, respectively, the adsorption capacity of $MnFe_2O_4$ nanoparticles for Hg^0 increased from 7.68 μg/g to 16.27 μg/g at the adsorption temperature of 30–50 ˚C. With the further rise of the adsorption temperature, the adsorption capacity of Hg^0 began to decline, and the adsorption capacity was only 8.0 μg/g at the adsorption temperature of 120 ˚C. This could be due to the fact that the adsorption of Hg^0 by $MnFe_2O_4$ nanoparticles was both physical and chemical adsorption mechanism, and the high temperature would cause the desorption of adsorbed Hg^0, and decrease the adsorption capacity, so the high temperature was not conducive to the physical adsorption. Therefore, the temperature of 50 ˚C was the optimum temperature for adsorption.

3.4 Effect of space velocity on the performance of mercury adsorption

In this experiment, the space velocity was varied by adjusting the flow rate of the simulated flue gas and other experimental conditions were kept constants. When the permeation temperature and the adsorption temperature were controlled at 40 ˚C and 50 ˚C, respectively, four gas flow rates (30 mL/min, 40 mL/min, 50 mL/min, and 60 mL/min) were set, and four space velocities were obtained by calculating 3.6×10^4 h^{-1}, 4.8×10^4 h^{-1}, 6.0×10^4 h^{-1}, and 7.0×10^4 h^{-1} via equation. The adsorption capacities of $MnFe_2O_4$ nanoparticles for Hg^0 at different space velocities were revealed in Fig 5 (S4 Table). It could be seen from the figure that, when the space velocity was increased from 3.6×10^4 h^{-1} to 4.8×10^4 h^{-1}, a large increase of the adsorption capacity for Hg^0 onto $MnFe_2O_4$ nanoparticles occurred. A reduction of adsorption capacity began to occur when the space velocity was greater than 4.8×10^4 h^{-1}, which indicated that the space velocity affected the performance of $MnFe_2O_4$ nanoparticles for the removal of mercury. The simulated flue gas would have a reduced contact time with the $MnFe_2O_4$ nanoparticles due to the rise in space velocity, and the chances of the $MnFe_2O_4$ nanoparticles capturing Hg^0 would be reduced, thus leading to a decline of adsorption capacity. Therefore, an airspeed lower than 4.8×10^4 h^{-1} was chosen to be more favorable for Hg^0 capture by $MnFe_2O_4$ nanoparticles.

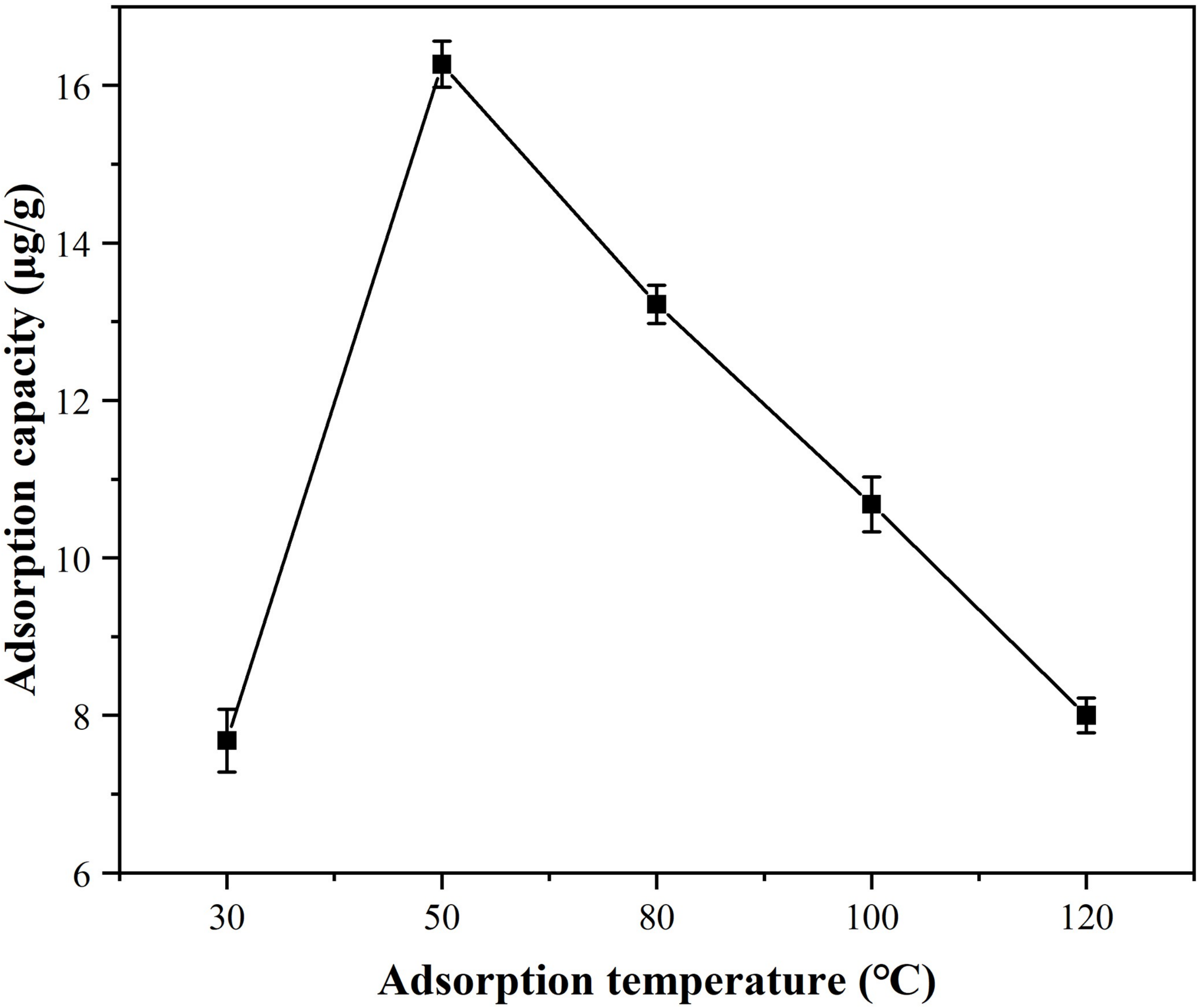

Fig 4. Adsorption capacity of $MnFe_2O_4$ nanoparticles for Hg^0 at different adsorption temperatures under permeation temperature of 40 ˚C and space velocity of 4.8×10^4 h^{-1}.

https://doi.org/10.1371/journal.pone.0304333.g004

3.5 Variation in adsorption capacity at different mercury permeation temperatures

Fig 6 (S5 Table) presented a trend of the adsorption capacity of $MnFe_2O_4$ nanoparticles for Hg^0 at different mercury permeation temperatures under space velocity of 4.8×10^4 h^{-1} and adsorption temperature of 50 ˚C. The $MnFe_2O_4$ nanoparticles exhibited a relatively larger adsorption capacity in all three permeation temperature ranges. As the permeation temperature rose, a large increase of adsorption capacity was observed. This was probably attributed to the fact that the increase of the concentration gave the adsorbent an increased opportunity to contact with Hg^0, which led to an increase of adsorption capacity. And this trend was also important in the practical application of coal-fired power plants, where the amount of adsorbent could be varied according to the actual needs of the plant.

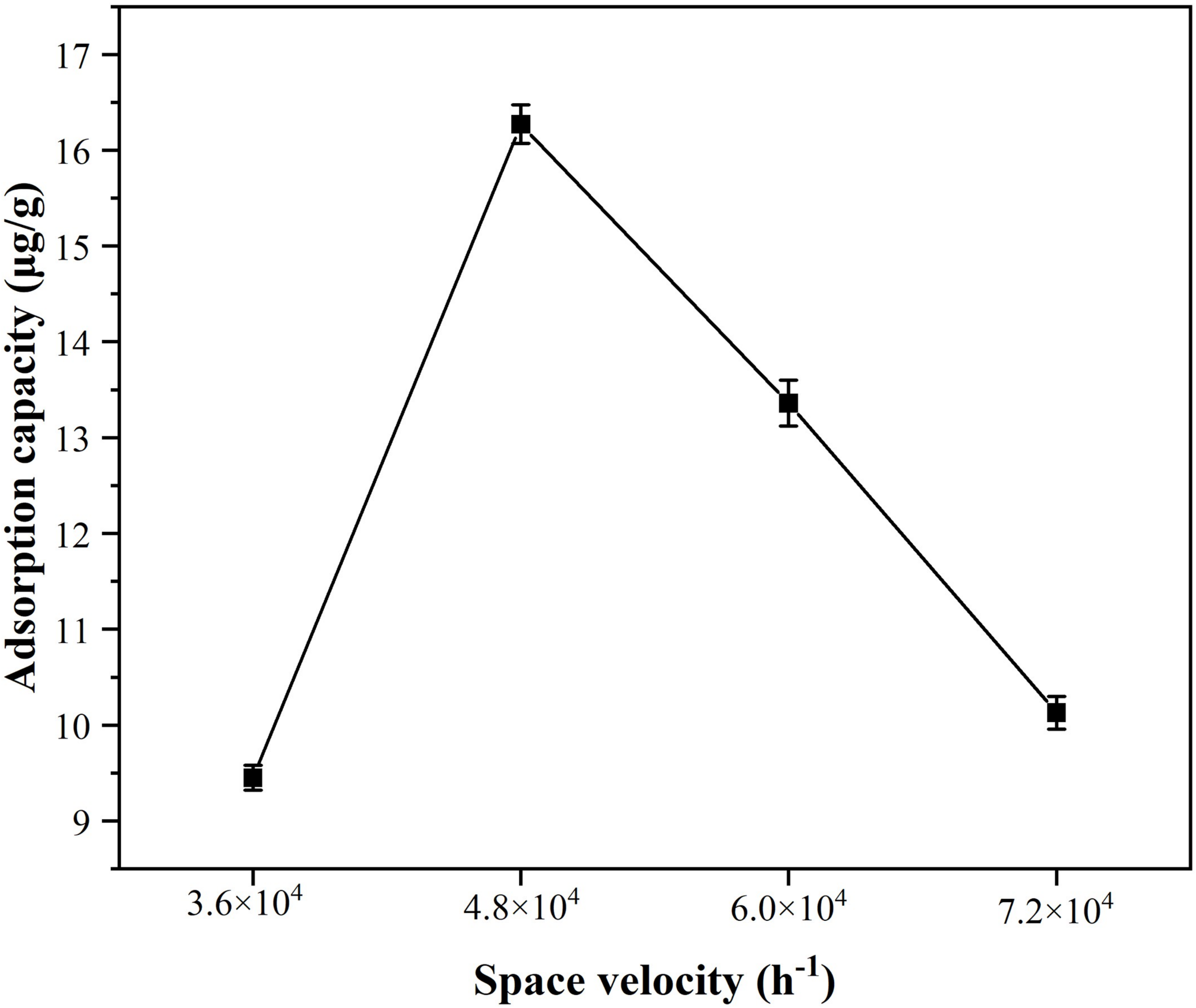

Fig 5. Effect of the space velocity on the performance of $MnFe_2O_4$ nanoparticles for Hg^0 removal under permeation temperature of 40 ˚C and the adsorption temperature of 50 ˚C.

https://doi.org/10.1371/journal.pone.0304333.g005

Compared with the previously reported articles related to mercury adsorption in gases (Table 1), the preparation method of $MnFe_2O_4$ nanoparticles proposed in this paper was low cost and easy to operate. In addition, the $MnFe_2O_4$ nanoparticles had better adsorption performance and short adsorption time, the biggest advantage was that $MnFe_2O_4$ could utilize its own magnetism to realize magnetic separation and recycling after adsorption, which effectively avoided secondary pollution.

3.6 Characterization of $MnFe_2O_4$ nanoparticles before and after adsorption

The magnetic properties of the $MnFe_2O_4$ nanoparticles before and after adsorption of Hg^0 were displayed in Fig 7. Obviously, the saturation magnetization of fresh $MnFe_2O_4$ nanoparticles was 79.53 $A{\cdot}m^2/kg$, after adsorption of Hg^0, the saturation magnetization

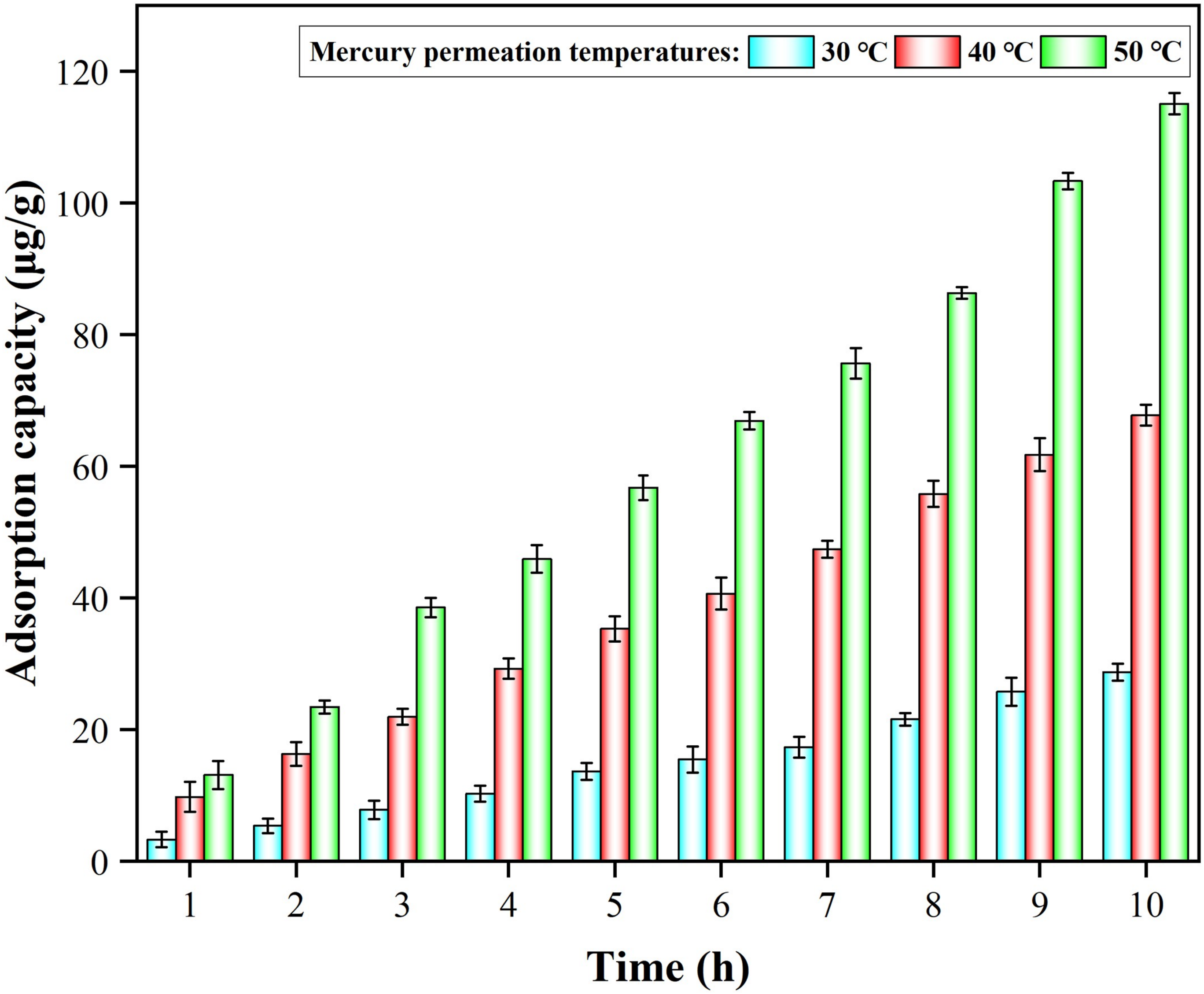

Fig 6. Effect of permeation temperature on Hg^0 removal by $MnFe_2O_4$ nanoparticles under space velocity of 4.8×10^4 h^{-1} and adsorption temperature of 50 ˚C.

https://doi.org/10.1371/journal.pone.0304333.g006

Table 1. Comparison of mercury adsorption from gases by as-prepared $MnFe_2O_4$ nanoparticles with other reported materials.

Adsorbing material	Initial Hg^0 concentration	Adsorption time (min)	Adsorption performance	References
Powdered activated carbon	500 μg/m^3	/	0.278 mg/g	[34]
Sulfurizing activate carbon	/	120	1227.5μg/g	[35]
Se/SiO_2 adsorbent	130 μg/m^3	14,400	101.04 mg/g	[36]
Fly ash	12.58 μg/m^3	180	0.005 mg/g	[37]
$MnFe_2O_4$	1.2 mg/m^3	60	16.27 μg/g	This work

https://doi.org/10.1371/journal.pone.0304333.t001

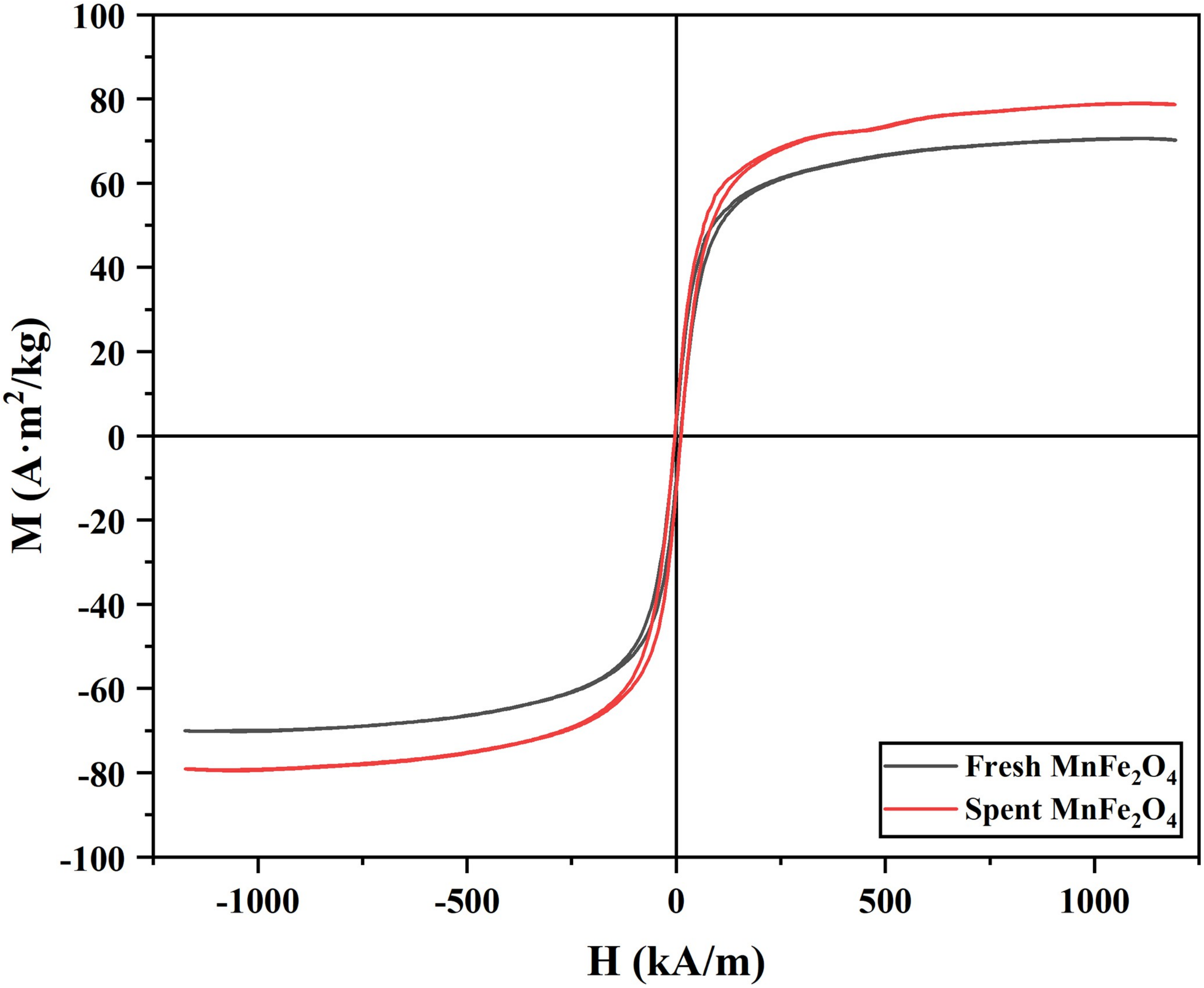

Fig 7. Hysteresis loops of $MnFe_2O_4$ nanoparticles before and after adsorption.

https://doi.org/10.1371/journal.pone.0304333.g007

intensity of the $MnFe_2O_4$ nanoparticles decreased to 70.21 $A \cdot m^2/kg$. Although the magnetic properties of the $MnFe_2O_4$ nanoparticles were slightly reduced, the overall saturation magnetization intensity of the $MnFe_2O_4$ nanoparticles was still very superior, and gas-solid separation could be achieved by magnetic separation, which avoided secondary pollution.

Fig 8 showed the SEM morphology of the $MnFe_2O_4$ nanoparticles after adsorption of Hg^0. It could be seen that there was a slight agglomeration of the adsorbed $MnFe_2O_4$ nanoparticles with no significant change in the morphology compared with Fig 1A. This demonstrated that the adsorption of Hg^0 by $MnFe_2O_4$ nanoparticles did not damage the themselves structure of the nanomaterials, which also indicated the possibility of recycling. The EDS plot revealed that the adsorbed materials contained the four elements Mn, Fe, O, and Hg, which demonstrated that Hg^0 was successfully adsorbed onto the adsorbent of $MnFe_2O_4$ nanoparticles [38].

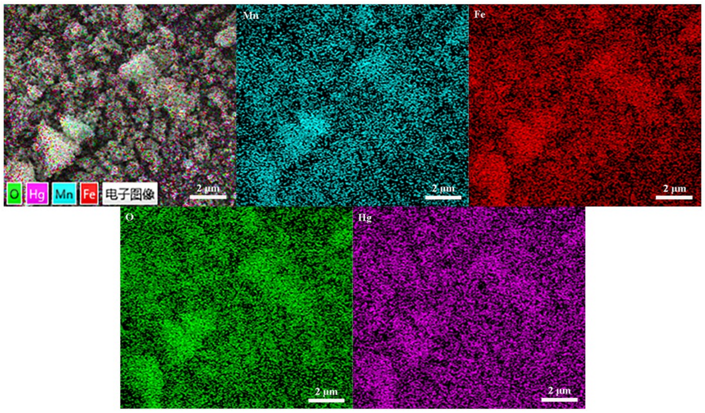

Fig 8. EDS plot of $MnFe_2O_4$ nanoparticles after adsorption.

https://doi.org/10.1371/journal.pone.0304333.g008

3.7 TG analyses of $MnFe_2O_4$ nanoparticles before and after adsorption

To further investigate the mechanism of Hg^0 removal before and after adsorption, TG analyses were performed on fresh and spent $MnFe_2O_4$ nanoparticles. As could be seen from Fig 9, the $MnFe_2O_4$ nanoparticles have about 1.7% mass loss below 140 ˚C, which was attributed to the loss of free water. At 140 ˚C-614 ˚C, fresh nanoparticles showed a mass loss of 3.7%, which might be caused by the evaporation of bound water in the nanomaterials and the combustion breakdown of part of the carbon skeleton. The mass loss of the spent nanoparticles was more than 1.3% compared with the fresh nanoparticles, which could be due to the desorption of the adsorbed mercury species. When the temperature exceeded 140 ˚C, the adsorbed Hg^0 on the $MnFe_2O_4$ nanoparticles was gradually thermally desorbed out, which indicated the presence of physical adsorption in the adsorption process. A significant mass loss was also observed in the range of 400 ˚C-600 ˚C, which was due to the decomposition of HgO, demonstrating the chemisorption of Hg^0 by the $MnFe_2O_4$ nanoparticles [6, 13, 39].

4. Conclusion

In this project, magnetic $MnFe_2O_4$ nanoparticles were prepared by the rapid combustion method, and the effects of absolute alcohol volume and calcination temperature on magnetic properties and average grain size were investigated during the preparation process. The adsorption effects of different experimental conditions on Hg^0 were examined by a fixed-bed experimental system. The experimental results revealed that the average particle size and the saturation magnetization of $MnFe_2O_4$ nanoparticles prepared at the calcination temperature of 500 ˚C with 30 mL of absolute ethanol were 25.3 nm and 79.53 $A{\cdot}m^2/kg$, and they exhibited the excellent adsorption capacity of 16.27 μg/g for Hg^0 at adsorption temperature of 50 ˚C and a space velocity of 4.8×10^4 h^{-1}. The comparison of the saturation magnetization intensity before and after adsorption displayed the magnetic stability of the $MnFe_2O_4$ nanoparticles after adsorption, which facilitated the separation and reuse in subsequent experiments. EDS and TG plots demonstrated the successful adsorption of Hg^0 onto the $MnFe_2O_4$ nanoparticles with the formation of the mercury compound as HgO, and the presence of both physical and chemical adsorption.

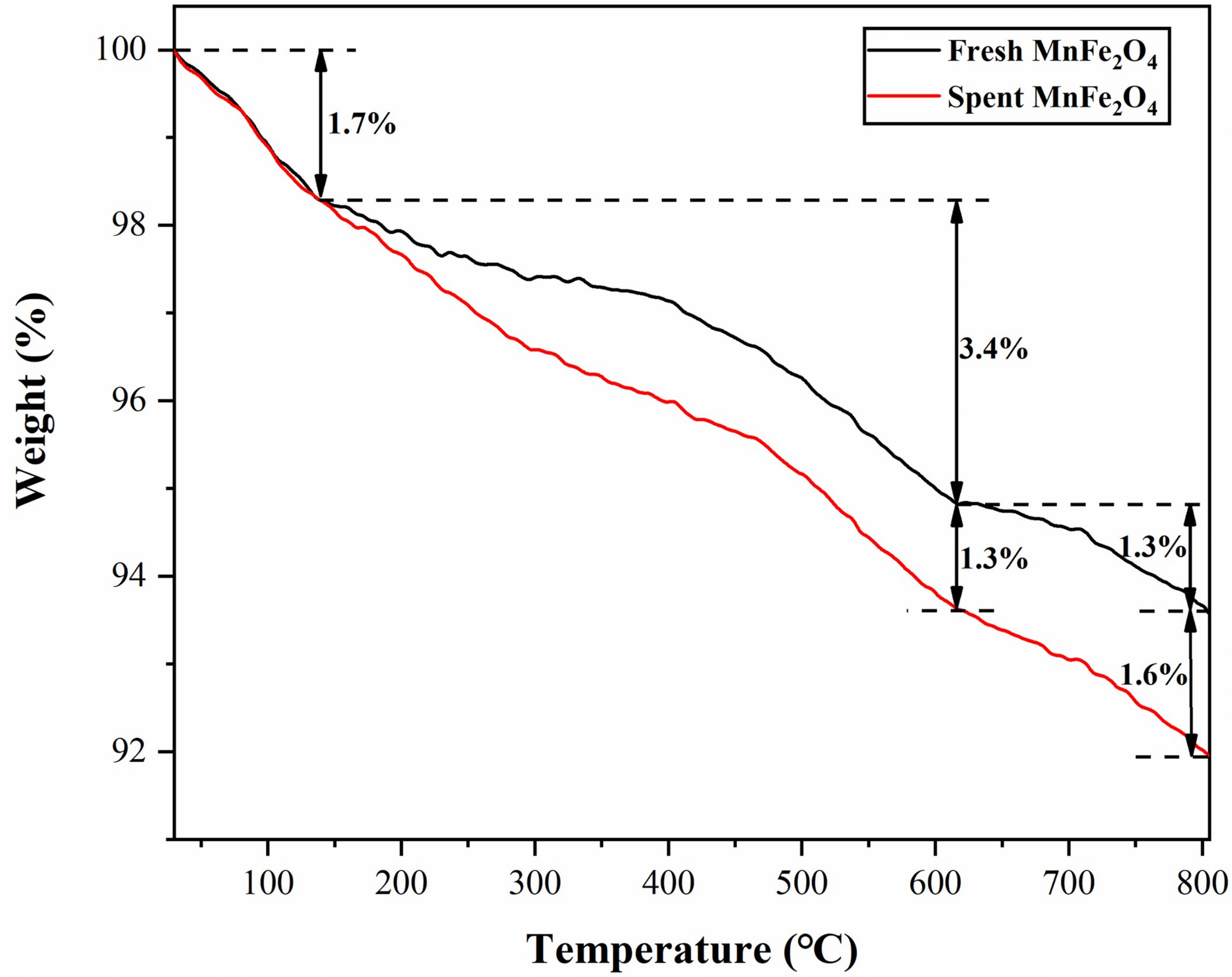

Fig 9. TG curves of the fresh and the spent $MnFe_2O_4$ nanoparticles.

https://doi.org/10.1371/journal.pone.0304333.g009

Supporting information

S1 Fig. SEM morphology of magnetic $MnFe_2O_4$ nanoparticles obtained by calcination at 500 ˚C for 30 mL of absolute ethanol for 2 h.
(TIF)

S2 Fig. TEM image of magnetic $MnFe_2O_4$ nanoparticles obtained by calcination at 500 ˚C for 30 mL of absolute ethanol for 2 h.
(BMP)

S3 Fig. XRD pattern of magnetic $MnFe_2O_4$ nanoparticles obtained by calcination at 500 ˚C for 30 mL of absolute ethanol for 2 h.
(TIF)

S4 Fig. XPS spectra of magnetic $MnFe_2O_4$ nanoparticles obtained by calcination at 500 ˚C for 30 mL of absolute ethanol for 2 h.
(TIF)

S1 Table. Adsorption data of Hg^0 by $MnFe_2O_4$ nanoparticles prepared with various alcohol volumes under permeation temperature of 40 ˚C, space velocity of 4.8×10^4 h^{-1}, and adsorption temperature of 30 ˚C.
(DOCX)

S2 Table. Adsorption data of Hg^0 by $MnFe_2O_4$ nanoparticles prepared at different calcination temperatures under permeation temperature of 40 ˚C, space velocity of 4.8×10^4 h^{-1}, and adsorption temperature of 30 ˚C.
(DOCX)

S3 Table. Adsorption capacity of $MnFe_2O_4$ nanoparticles for Hg^0 at different adsorption temperatures under permeation temperature of 40 ˚C and space velocity of 4.8×10^4 h^{-1}.
(DOCX)

S4 Table. Effect of the space velocity on the performance of $MnFe_2O_4$ nanoparticles for Hg^0 removal under permeation temperature of 40 ˚C and the adsorption temperature of 50 ˚C.
(DOCX)

S5 Table. Effect of permeation temperature on Hg^0 removal by $MnFe_2O_4$ nanoparticles under space velocity of 4.8×10^4 h^{-1} and adsorption temperature of 50 ˚C.
(DOCX)

Author Contributions

Conceptualization: Lei Sun, Xiajun Zhang.

Data curation: Lei Sun, Zhou Wang.

Formal analysis: Xiajun Zhang.

Funding acquisition: Zhou Wang.

Investigation: Lei Sun, Xiajun Zhang.

Methodology: Lei Sun, Xiajun Zhang, Zhou Wang.

Project administration: Min Liu.

Resources: Min Liu.

Supervision: Zhou Wang, Min Liu.

Writing – original draft: Lei Sun, Xiajun Zhang.

Writing – review & editing: Zhou Wang, Min Liu.

References

1. Pirarath R, Souwaileh AA, Wu JJ, Anandan S. Amino acid-induced exfoliation of MoS_2 nanosheets through hydrothermal method for the removal of mercury. Inorg. Chim. Acta 2024; 561: 121855. https://doi.org/10.1016/j.ica.2023.121855
2. Meng FY, Yang ZQ, Yang JP, Leng LJ, Qu WQ, Wen PZ, et al. Cupric ion stabilized iron sulfide as an efficient trap with hydrophobicity for elemental mercury sequestration from flue gas. Sep. Purif. Technol. 2024; 330: 125385. https://doi.org/10.1016/j.seppur.2023.125385

3. Li Y, Wang Y, Liu YX, Zhao YC. Clean Modification of Carbon-Based Materials Using Hydroxyl Radicals and Preliminary Study on Gaseous Elemental Mercury Removal. Energy Fuels 2023; 37: 5953–5960. https://doi.org/10.1021/acs.energyfuels.2c04172
4. Zhang L, Zheng Y, Li GL, Gao JJ, Li R, Yue T. Review on magnetic adsorbents for removal of elemental mercury from coal combustion flue gas. Environ. Res. 2024; 243: 117734. https://doi.org/10.1016/j.envres.2023.117734 PMID: 38029827
5. Xu HM, Hong QY, Zhang ZY, Cai XL, Fan YR, Liu ZS, et al. SO_2-Driven In Situ Formation of Super-stable $Hg_3Se_2Cl_2$ for Effective Flue Gas Mercury Removal. Environ. Sci. Technol. 2023; 57: 5424–5432. https://doi.org/10.1021/acs.est.2c09640 PMID: 36939455
6. Wang FJ, Tang TH, Zhang RT, Cheng ZH, Wu J, He P, et al. Magnetically recyclable CoS-modified graphitic carbon nitride-based materials for efficient immobilization of gaseous elemental mercury. Fuel 2022; 326: 125117. https://doi.org/10.1016/j.fuel.2022.125117
7. Su JC, Yang JC, Zhang MK, Gao MK, Zhang YQ, Gao MY, et al. Improvement mechanism of Ru species on Hg^0 oxidation reactivity over V_2O_5/TiO_2 Catalyst: A density functional theory study. Chem. Eng. Sci. 2023; 274: 118689. https://doi.org/10.1016/j.ces.2023.118689
8. Zhang XP, Wei YY, Zhang LH, Wang XX, Zhang N, Bao JJ, et al. Self-template synthesis of $CuCo_2O_4$ nanosheet-based nanotube sorbent for efficient Hg^0 removal. Sep. Purif. Technol. 2023; 313: 123432. https://doi.org/10.1016/j.seppur.2023.123432
9. Ding Z, Yang C, Zhang H, Mei J, Wang J, Yang SJ. New utilizations of natural $CuFeS_2$ as the raw material of Cu smelting for recovering Hg^0 from Cu smelting flue gas. Fuel 2023; 341: 126997. https://doi.org/10.1016/j.fuel.2022.126997
10. Shen FH, He SD, Li JY, Wang PS, Liu H, Xiang KS. Novel insight into elemental mercury removal by cobalt sulfide anchored porous carbon: Phase-dependent interfacial activity and mechanisms. Fuel 2023; 331: 125740. https://doi.org/10.1016/j.fuel.2022.125740
11. Dong S, Wang JH, Li CQ, Liu H, Gao ZY, Wu CC, et al. Simultaneous catalytic oxidation mechanism of NO and Hg^0 over single-atom iron catalyst. Appl. Surf. Sci. 2023; 609: 155298. https://doi.org/10.1016/j.apsusc.2022.155298
12. Zheng W, Zhou XY, Na YY, Yang JP, Hu YC, Guo QJ, et al. Facile fabrication of regenerable spherical $La_{0.8}Ce_{0.2}MnO_3$ pellet via wet-chemistry molding strategy for elemental mercury removal. Chem. Eng. J. 2024; 479: 147659. https://doi.org/10.1016/j.cej.2023.147659
13. Yu Q, Yang XJ, Dong YH, Qian Z, Yuan B, Fu D. Microwave-boosted elemental mercury removal using natural low-grade pyrolusite. Chem. Eng. J. 2023; 455: 140700. https://doi.org/10.1016/j.cej.2022.140700
14. Ye D, Gao SJ, Wang YL, Wang XX, Liu X, Liu H, et al. New insights into the morphological effects of MnO_x-CeO_x binary mixed oxides on Hg^0 capture. Appl. Surf. Sci. 2023; 613: 156035. https://doi.org/10.1016/j.apsusc.2022.156035
15. Dou ZF, Wang Y, Liu YX, Zhao YC, Huang RK. Enhanced adsorption of gaseous mercury on activated carbon by a novel clean modification method. Sep. Purif. Technol. 2023; 308: 122885. https://doi.org/10.1016/j.seppur.2022.122885
16. You SW, Liao HY, Tsai CY, Wang C, Deng JG, His HC. Using novel gold nanoparticles deposited activated carbon fiber cloth for continuous gaseous mercury recovery by electrothermal swing system. Chem. Eng. J. 2022; 431: 134325. https://doi.org/10.1016/j.cej.2021.134325
17. Zhou WJ, Liu M, Zhang SS, Su GD, Jin X, Liu RJ. Hg^0 chemisorption of magnetic manganese cobalt nano ferrite from simulated flue gas. Phys. Scripta 2024; 99: 035003. https://doi.org/10.1088/1402-4896/ad2248
18. Silva BFD, Mafra LC, Zanella DSI, Luiz DG, Rhoden BRC. A DFT theoretical and experimental study about tetracycline adsorption onto magnetic graphene oxide. J. Mol. Liq. 2022; 353: 118837. https://doi.org/10.1016/j.molliq.2022.118837
19. Weng XL, Chen W, Cai WL, Owens G, Chen ZL. Synthesis of ferroferric oxide@silicon dioxide/cobalt-based zeolitic imidazole frameworks for the removal of doxorubicin hydrochloride from wastewater. J. Colloid Interf. Sci. 2022; 624: 108–120. https://doi.org/10.1016/j.jcis.2022.05.150 PMID: 35660880
20. Gürbüz MU, Elmacı G, Ertürk AS. In situ deposition of silver nanoparticles on polydopamine-coated manganese ferrite nanoparticles: Synthesis, characterization, and application to the degradation of organic dye pollutants as an efficient magnetically recyclable nanocatalyst. Appl. Organomet. Chem. 2021; 35: e6284. https://doi.org/10.1002/aoc.6284
21. Ertürk AS, Elmacı G, Gürbüz MU. Reductant free green synthesis of magnetically recyclable $MnFe_2O_4@SiO_2$-Ag core-shell nanocatalyst for the direct reduction of organic dye pollutants. Turk. J. Chem. 2021; 45: 1968–1979. https://doi.org/10.3906/kim-2108-2 PMID: 38144589

22. Gürbüz MU, Koca M, Elmacı G, Ertürk AS. In situ green synthesis of $MnFe_2O_4$@EP@Ag nanocomposites using Epilobium parviflorum green tea extract: An efficient magnetically recyclable catalyst for the reduction of hazardous organic dyes. Appl. Organomet. Chem. 2021; 35: e6230. https://doi.org/10.1002/aoc.6230

23. Elmacı G, Özgenç G, Kurz P, Zumreoglu-Karan B. Enhanced water oxidation performances of birnessite and magnetic birnessite nanocomposites by transition metal ion doping. Sustain. Energ. Fuels 2020; 4: 3157–3166. https://doi.org/10.1039/D0SE00301H

24. Elmacı G, Frey CE, Kurz P, Zümreoğlu-Karan B. Water oxidation catalysis by using nano-manganese ferrite supported 1D-(tunnelled), 2D-(layered) and 3D-(spinel) manganese oxides. J. Mater. Chem. A 2016; 4: 8812–8821. https://doi.org/10.1039/C6TA00593D

25. Dhal JP, Sahoo A, Acharya AN. Flake shaped $ZnFe_2O_4$ nanoparticles: synthesis, characterization and visible light induced photocatalytic study. Emerg. Mater. Res. 2023; 12: 1–9. https://doi.org/10.1680/jemmr.22.00184

26. Nhlapo TA, Msomi JZ, Moyo T. Temperature-dependent magnetic behavior of Mn-Mg spinel ferrites with substituted Co, Ni & Zn, synthesized by hydrothermal method. J. Mol. Struct. 2021; 1245: 131042. https://doi.org/10.1016/j.molstruc.2021.131042

27. Yue Y, Zhang XJ, Zhao SH, Wang XY, Wang J, Liu RJ. Construction of Label-Free Electrochemical Biosensing System with Magnetic-Induced Self-Assembly for the Detection of EGFR Glycoprotein. Vacuum 2024; 222: 112975. https://doi.org/10.1016/j.vacuum.2024.112975

28. Zhang YL, Wang J, Liu M, Ni Y, Yue Y, He DW, et al. Magnetically induced self-assembly electrochemical biosensor with ultra-low detection limit and extended measuring range for sensitive detection of HER2 protein. Bioelectrochemistry 2024; 155: 108592. https://doi.org/10.1016/j.bioelechem.2023.108592 PMID: 37925821

29. Yue Y, Ouyang HZ, Ma MY, Yang YP, Zhang HD, He AL, et al. Cell-free and label-free nucleic acid aptasensor with magnetically induced self-assembly for the accurate detection of EpCAM glycoprotein. Microchim. Acta 2024; 191: 64. https://doi.org/10.1007/s00604-023-06117-y PMID: 38157059

30. Ni Y, Deng P, Yin RT, Zhu ZY, Ling C, Ma MY, et al. Effect and mechanism of paclitaxel loaded on magnetic Fe_3O_4@$mSiO_2$-NH_2-FA nanocomposites to MCF-7 cells. Drug Deliv. 2023; 30: 64–82. https://doi.org/10.1080/10717544.2022.2154411 PMID: 36474448

31. Deivatamil D, John AMM, Thiruneelakandan R, Joseph PJ. Fabrication of $MnFe_2O_4$ and Ni: $MnFe_2O_4$ nanoparticles for ammonia gas sensor application. Inorg. Chem. Commun. 2021; 123: 108355. https://doi.org/10.1016/j.inoche.2020.108355

32. Ling C, Wang Z, Ni Y, Zhu ZY, Cheng ZH, Liu RJ. Superior adsorption of methyl blue on magnetic Ni-Mg-Co ferrites: Adsorption electrochemical properties and adsorption characteristics. Environ. Prog. Sustain. 2022; 41: e13923. https://doi.org/10.1002/ep.13923

33. Pan S, Huang W, Yu QM, Liu X, Liu YH, Liu RJ. A rapid combustion process for the preparation of $Ni_xCu_{(1-x)}Fe_2O_4$ nanoparticles and their adsorption characteristics of methyl blue. Appl. Phys. A-Mater. 2019; 125: 88. https://doi.org/10.1007/s00339-019-2390-6

34. Lin HY, Yuan CS, Chen WC, Hung CH. Determination of the adsorption isotherm of vapor-phase mercury chloride on powdered activated carbon using thermogravimetric analysis. J. Air Waste Manage. 2006; 56: 1550–1557. https://doi.org/10.1080/10473289.2006.10464561 PMID: 17117740

35. Wu GF, Xu MR, Liu QC, Yang J, Ma DR, Lu CF, et al. Micromechanism of sulfurizing activated carbon and its ability to adsorb mercury. Appl. Phys. A-Mater. 2013; 113: 389–395. https://doi.org/10.1007/s00339-013-7934-6

36. Xiao RH, Zhang YL, Wei SZ, Chuai X, Cui X, X Z, et al. A high efficiency and high capacity mercury adsorbent based on elemental selenium loaded SiO_2 and its application in coal-fired flue gas. Chem. Eng. J. 2023; 453: 139946. https://doi.org/10.1016/j.cej.2022.139946

37. Xu WQ, Wang HR, Zhu TY, Kuang JY, Jing PF. Mercury removal from coal combustion flue gas by modified fly ash. J. Environ. Sci. 2013; 25: 393–398. https://doi.org/10.1016/s1001-0742(12)60065-5 PMID: 23596961

38. Ma YP, Xu TF, Zhang XJ, Fei ZH, Zhang HZ, Xu HM, et al. Manganese bridge of mercury and oxygen for elemental mercury capture from industrial flue gas in layered Mn/MCM-22 zeolite. Fuel 2021; 283: 118973. https://doi.org/10.1016/j.fuel.2020.118973

39. Luo ZF, You L, Wu J, Song YB, Ren SY, Jia T, et al. Selenium ligands doped ZnS for highly efficient immobilization of elemental mercury from coal combustion flue gas. Chem. Eng. J. 2021; 420: 129843. https://doi.org/10.1016/10.1016/j.cej.2021.129843